OVERVIEW TO THE ESA-EMAP PROJECT: CHARACTERIZATION OF SRM PLUMES WITH ALUMINA PARTICULATE IN SUBSCALE TESTING

Dominik Saile[1*], *Dirk Kerkhoff*[1], *Viktor Kühl*[1], *Lars Steffens*[1], *Ali Gülhan*[1],
Manfred Beversdorff[2], Wolfgang Förster, Chris Willert[2],
Stefania Carlotti[3], Filippo Maggi[3],
Mattias Liljedahl[4], Niklas Wingborg[4], Jeroen van den Eynde[5], Tobias Langener[5]

DLR - German Aerospace Center
[1]Institute of Aerodynamics and Flow Technology
[1]Supersonic and Hypersonic Technologies Department (DLR AS-HYP)
[2]Institute of Propulsion Technology
[2]Engine Measurement Systems (DLR AT-OTM)
Cologne, Germany
[*]Dominik.Saile@dlr.de

[3]Politecnico di Milano (PoliMi/SPLab)
Department of Aerospace Science and Technology
Milan, Italy

[4]Swedish Defence Research Agency (FOI)
Department of Energetic Materials
Norra Sorunda, Sweden

[5]European Space Agency (ESA/ESTEC)
Noordwijk, Netherlands

ABSTRACT

The current paper provides an overview of the ESA-EMAP project. This project pursues activities regarding the experimental modeling of alumina particulates in solid boosters. The issue regards the particles residing in the atmosphere after the passage of a launch vehicle with solid rocket propulsion, which might contribute to local and overall ozone depletion. The question is to what extent since the particle size distribution left behind is essentially unclear. For this reason, the ESA-EMAP investigations focus on the characterization of the solid exhaust plume properties for well-defined combustion chamber conditions. Thus, details of the rocket motor assembly, of the developed solid propellant grains and of first measurement results are provided. The paper presents technical findings concerning the rocket motors and reveals aspects to the feasibility of the applied measurement techniques.

1. INTRODUCTION

ESA-EMAP is a project initiated by the *European Space Agency* to pursue activities regarding the experimental modeling of alumina particulates in solid boosters. On the contractor side, the team consists of the *German Aerospace Center (DLR)*, the *Space Propulsion Lab (SPLab)* of the *Politecnico di Milano* and the *Department of Energetic Materials* of the *Swedish Defence Research Agency (FOI)*. As lead, the DLR department of *Supersonic and Hypersonic and Hypersonic Technologies Department (AS-HYP)* is in charge of project management, but also responsible for the execution of the tests and for the application of numerous measurement techniques (see below for DAQ , PIV, DIPSD, spectroscopic measurements, HSS, APS, Gardon Gauge, IR-thermography). The *DLR* department *Engine Measurement Systems (AT-OTM)* conducted *laser-2-focus (L2F)* measurements, while the *SPLab* of *Polimi* took over the responsibility of developing a *rocket plume collector (RPC)* probe and activities regarding the characterization of the propellant. The

propellant grain under discussion was developed, investigated and manufactured by *FOI*.

The main driver for the activities is related to the uncertainty and discrepancy of studies regarding the impact of the alumina particles emitted by solid rocket motors (SRMs) on the ozone depletion of the stratosphere. Heterogeneous reactions on the surface of alumina particles, in particular chlorine activation reactions, are considered as a significant mechanism potentially doubling the change in annually averaged total ozone attributed to the emission SMRs [1]. Of major concern is the particle size distribution. In models regarding the global ozone depletion, chlorine activation reaction is sensitive to the surface area fraction of the particles [2].

It is stated of Schmid et al. [1] that for small SRMs, the ozone loss due to reactions on alumina emissions is comparable to the ozone loss of the gas phase chlorine emissions alone. Ross et al. [3], on the other hand, found out that reactions on alumina have only an insignificant influence on stratospheric chemistry. The difference of this assessment is attributed to the difference of the measured alumina particle size distribution. The latter study [3] describes that less than a few hundredths of a percent of the alumina mass resides in the smallest particle size mode, while [1] found 8% of the total mass in submicron size range, which corresponds 37% of the total surface area.

The objective of the current study is now to shed light on the formation processes of alumina in solid propellant launcher. These activities take place in the frame of the CLEAN SPACE initiative, which has as overarching goal the reduction of environmental impacts of launch vehicles. In order to do so, it is necessary to quantify the actual emission induced by each launch. Thus, it is of importance to determine the plume conditions and its impact on the atmosphere and in more detail the formation, development and long-term presence in the atmosphere of alumina particulates and/or other aerosols. Note that particles in the exhaust plume also lead to a variety of technical challenges for space transportation such as increased heat loads, contamination of system-relevant surfaces or to radio-frequency interference. Such effects are reported in [4, 5, 6].

In the frame of ESA-EMAP, the objectives are to characterize the exhaust plume as extensively as possible with respect to the exhaust gas, the exhaust particles and the heat flux. However, the study at hand must be seen as a first step for further publications. It provides an overview to the methods applied, the materials used, and the approach taken. Another focus is on the technical aspects of the development of the rocket motor and with respect to the measurement techniques. For the latter, it was always the question if the corresponding measurement technique can cope with the harsh measurement environment and capture the targeted data. Concerning the motor, some of these technical questions are listed below. These are the questions that will be addressed in the paper at hand.

- Can the glow plug used for the ignition?
- Does the insulation material provide sufficient protection for the walls?
- Does the combustion chamber pressure evolve as predicted?
- Is tungsten suitable as material for the nozzles?
- Can PEEK be used as material for the heat flux measurements in the base region?
- Are the measurement methods applicable as intended?
- Is the reciprocal interference of various measurement methods limited and as predicted?

2. METHODS - TEST ENVIRONMENT

In the following, the test environment consisting of the *Vertical Test Section Cologne (VMK)*, the rocket motor, and as part of the rocket motor, the solid propellant grains are described.

2.1. Vertical Test Section Cologne (VMK)

The experiments are executed in the *Vertical Test Section Cologne (VMK)*. VMK [7, 8, 9] is a blow-down type wind tunnel featuring a vertical and free test section for tests in the subsonic to supersonic range starting from Mach 0.5 up to 3.2. The current experiments were conducted with a subsonic nozzle featuring an exit diameter of $340\,\mathrm{mm}$.

2.2. Rocket Motor

A rocket motor was used for the execution of the experiments. This motor is shown in fig. 1 and, as it can be seen, it is integrated via an upstream support (1) in the subsonic wind tunnel nozzle (2). The rocket motor consists of the main casing of the motor (3), a bottom plate (4), a nozzle block (5a-5c) and a base plate (6). For the main tests, end burner grains (7) as introduced in section 2.3 are used. In this case, the void in the motor is filled with a dummy propellant (8). A hull (9) is put over the rocket motor and the gap between the motor and the hull is used for harnessing. For the case at hand, this is only the glow plug (10) for the ignition of the propellants. For the precursor measurement calibration tests, commercially available BATES grains are used.

The main casing (3) is made of inconel 718. For one part of the nozzle block (5a+5b), molybdenum is used while the nozzles themselves (5c) are made of tungsten. The nozzle block is the assembly group which is the most exposed to heat and pressure loads. One of the questions was how these components withstand the imposed loads. A discussion of which is part of the results in section 4.1.

Another objective was to take measurements at specified nozzle exit planes for realistic chamber pressure levels. For this reason, corresponding nozzles were developed. In total,

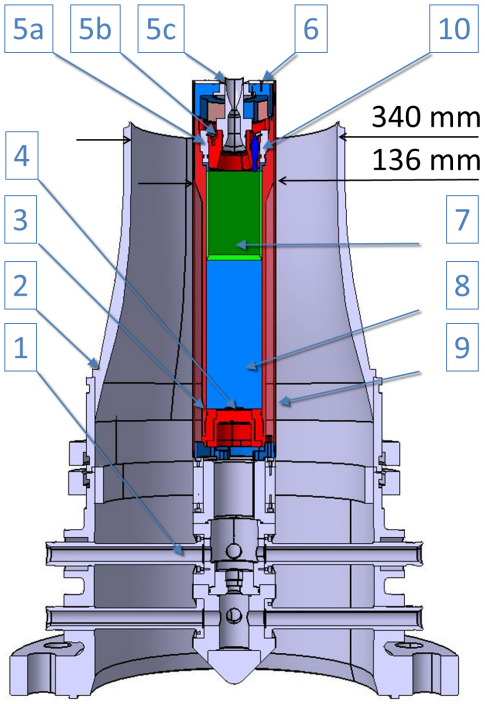

Fig. 1. Sketch of the wind tunnel model with rocket motor

9 different nozzles with different nozzle contours were manufactured with three different throat diameters and three different expansion ratios. In the order of ascending chamber pressure levels, the throat diameters are $d_{th} = 7.75, 6.57$ and $5.74\,\mathrm{mm}$. The three expansion ratios are 14.4, 2.1, and 1.0, which are equivalent to an exit Mach number of 3.23, 2.1 and about 1, respectively.

Note that the nozzles with the largest expansion ratio are used as baseline. In other words, the contours of the various Mach numbers (for one throat diameter) are essentially the same except for the fact that they are truncated at the locations to reach corresponding Mach numbers. The nozzle type corresponds to a truncated ideal contour (TIC) nozzle designed by means of the method of characteristics [10], without compensation of the boundary layer displacement. It was determined by means of the *RPA - Rocket Propulsion Analysis* software [11]. The exit angle for the nozzle with the largest expansion ratio is $\leq 0.5°$.

Despite being different with respect to the contour, the outer silhoutte of the wind tunnel model remains the same for all investigated nozzle configurations. In other words, similarity is given with respect to the outer geometry independently of the internal contour of the nozzle. This is visualized in fig. 2. Apart from the geometric similarity, this approach is also advantageous for the setup of the measurement systems: the region of interest is fixed at a location downstream from the nozzle exit and the measurement equipment does not require a readjustment when changing the nozzle configuration.

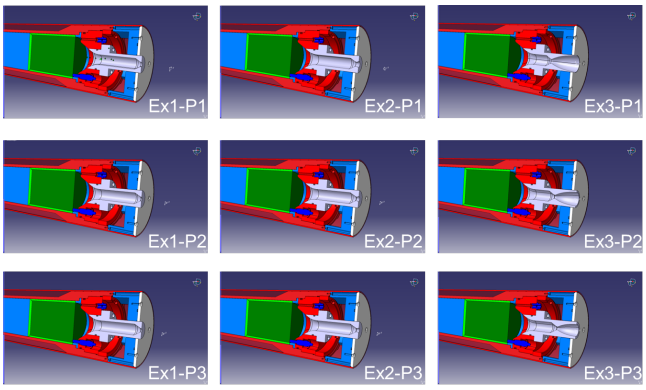

Fig. 2. Nozzle lengths with respect to the base plate

The main focus of the study is not necessarily on the interaction phenomena such as in previous works [12, 13, 14, 15, 16]. This would also be difficult taking into account the influence of the protection shield for the RPC probe as introduced in section 3, which significantly influences - when used - the near-wake flow. Instead the overarching study objective lays on the exhaust plume, and for this study in particular, on the rocket motor and the feasibility of measurement techniques. For this reason, the relatively large diameter/area ratio between the nozzle exit and the wind tunnel model appears justified.

2.3. Solid Propellant Grains

The solid propellant grains are of the end burning type. The idea behind was that end burners typically satisfy the requirement for a constant pressure evolution over time. The intention of which is to aim for constant conditions for all measurement techniques over one run.

In that frame, FOI has developed three different solid propellants:

- HTPB1814 with 18% aluminum and 14% HTPB,
- HTPB0514 with 5% aluminum and 14% HTPB and
- HTPB0014Al2O3 with 14% HTPB and with 5% Al_2O_3 as inert filler.

Note that HTPB stands for hydroxyl-terminated polybutadiene. For the case at hand, HTPB1814 is intended for the investigation of a realistic booster plume comparable to the Ariane 5 configuration, HTPB0514 is less smoky and is being used for investigations where optical transparency is required (e.g. PIV), and HTPB0014Al2O3 is intended for the validation of the particle size measurement approaches. Apart from Al_2O_3, the propellants developed are based on conventional ingredients such as ammonium perchlorate (AP) embedded in a HTPB based binder, similarly as used in Ariane 5 and Vega.

The composition of the HTPB based binder is shown in table 1. The binder composition is selected to be similar to what is used in state of the art solid rocket propellants. Two different batches of HTPB were used; HTPB R45HTLO from Cray Valley (for propellant batch no. G180243) and HTPB Polyvest from Evonik (for propellant batch no. G180245). The HTPBs have previously been evaluated by FOI are expected to produce materials with very similar behaviour. The reason for using two different batches was a shortage of material of the same batch for all the casts. It was decided to use HTPB Polyvest in one of the HTPB0514-batches since that composition was produced in duplicate. The batch of HTPB R45HTLO used has, according to the Cray Valley certificate of analysis, an OH-functionality of $0.80\,\mathrm{mmol/g}$. The batch of HTPB Polyvest used has, according to the test report from Evonik, a hydroxyl number of $48\,\mathrm{mgKOH/g}$. A NCO/OH-ratio of 0.8 was selected and the amount of Desmodur W needed was calculated to be $8.38\,\mathrm{phr}$ for the HTPB R45HTLO binder and $8.97\,\mathrm{phr}$ for the HTPB Polyvest binder.

Two brands of ammonium perchlorate were used. The first brand, from Switzerland Elektrochemie Turgi, type AMZ, with suitable particle size and morphology, was used as received. The second brand, from Trona, USA, type A, was grinded using a Sturtevant 4 inch Micronizer jet mill. Afterwards, the particle size and distribution were measured using a Malvern Mastersizer 2000. The particle size was reported for the 10th, 50th and 90th percentile of the volume fraction; low 10%, 50% and high 10% (shown as d_{10}, d_{50} and d_{90}) and the particle size span S was calculated as given in eq. (1). As a result, the measurement revealed a particle size of $d_{50} = 168\,\mu\mathrm{m}$ and a particle size span of $S = 1.1$ for the AMZ (used as received). The Trona jet milled AP featured $d_{50} = 7\,\mu\mathrm{m}$ and $S = 1.4$.

$$S = \frac{d_{90} - d_{10}}{d_{50}} \tag{1}$$

Since the measurements focus on the particles in the exhaust jet, the initial particle size of aluminum and alumina, meaning before being released and possibly burned (aluminum) in the combustion chamber, shall also be provided hereafter. For the (supposedly) inert filler, the alumina powder Amperit 740.065 by H.C. Starck was used and, for the other propellants, aluminum powder was added to the propellant. The diameter of alumina at a volume fraction 10%, 50% and 90% is $[d_{10}, d_{50}, d_{90}] = [\mathrm{min.}\ 11, 19-23, \mathrm{max.}\ 40]\,\mu\mathrm{m}$. The size span is then in the range between $S = 1.3$ and 1.5. The diameter of aluminum at volume fraction of a 50% is $d_{50} = 16.5\,\mu\mathrm{m}$ with a corresponding size span of S = 1.2.

Mixing and casting was executed under vacuum according to a predefined procedure. Then, all batches were cured at $70\,^{\circ}\mathrm{C}$ for 5 days. The respective propellant composition are shown in table 2. The volume fraction filler was between 73% and 74%. As a last step, an insulation consisting of HTPB, carbon black and BKF cured with Desmodur W was applied at the bottom and on the side walls (along the circumference) of the propellants. The weight of each grain was, depending on the propellant grain type, in the range between about $850\,\mathrm{g}$ and $890\,\mathrm{g}$.

All manufactured grains had densities within 1% of theoretical maximum density (TMD). The corresponding densities are shown in table 3. This table also contains the strand burner tests conducted by the SPLab team of PoliMi to determine the burn rates of the propellants. For that purpose, data correlation with data from the strand burner tests has been performed using the classical Vieille's law $r_b = ap^n$, where r_b is the burning rate, a and n are fitting parameters, and p is the pressure. Generally, the uncertainty bounds for a and n are $\sigma_a < 0.36$ and $\sigma_n < 0.42$, respectively.

3. METHODS

As introduced above, *Vertical Test Section Cologne (VMK)* is a blow-down type wind tunnel facility with an open test section. The combination of having the wind tunnel nozzle vertically aligned and featuring an open test section is advantageous for the current tests since it offers the space which is required for the highly instrumented experiments in the frame of ESA-EMAP. An overview of the measurement techniques and targeted quantities is given in table 4.

The image in Fig. 3 provides proof that the term 'highly instrumented' is justified. It shows the inside of VMK with the wind tunnel model integrated in the wind tunnel nozzle. The wind tunnel model mimics the base region of a launch vehicle. To simulate a flight-realistic exhaust plume, a solid rocket motor is integrated in the base model. The rocket motor expels the hot jet in the upward direction through a nozzle. Simultaneously, the wind tunnel provides an ambient flow at Mach 0.6. In other words, a co-flow between a cold ambient flow and a hot solid propellant exhaust jet is investigated.

For this reason, the wind tunnel model is surrounded with measurement equipment. Just downstream from the nozzle exit of the rocket motor, one can find the *rocket plume collector (RPC)* [25]. The RPC is used to collect particles for the determination of the particle size distribution. It is protected from the hot exhaust gas by a protective shield, which only opens for $0.5\,\mathrm{s}$ during each run. The aerodynamic particle sizer (APS) is even farther downstream and serves the same purpose by means of the scattering intensity of light on particles and by aerodynamic measurements. The heat flux is captured with two different methods: First, an infrared camera (IR) acquires the temperature evolution of the base, and second, a Gardon gauge points at the rocket exhaust plume to collect data of its heat flux radiation. The temperature of the rocket exhaust plume itself is assessed with spectroscopic measurements. Measurements by means of Fourier-transform infrared spectroscopy (FTIR) and by spectroscopy in the ultraviolet–visible range (UV-Vis) are conducted. Moreover,

Table 1. HTPB binder composition (in parts per 100 parts of rubber, phr), with NCO/OH ratio of 0.8

Chemical	Amount (phr)	Comment
HTPB R45HTLO or HTPB Polyvest	100	Pre-polymer
BKF	1.5	Antioxidant
DOA	25	Plasticizer
TEPAN	1	Bonding agent
Desmodur W	8.38 (R45HTLO) or 8.97 (Polyvest)	Curing agent

Table 2. Propellant composition

Component	HTPB1814 (%)	HTPB0514 (%)	HTPB0014Al2O3 (%)
HTPB binder	14	14	14
AP AMZ (coarse)	53.3	56.1	55.2
AP jet milled (fine)	14.2	24.4	25.3
Al	18	5	0
Al_2O_3	0	0	5
Fe_2O_3	0.5	0.5	0.5

Table 3. Propellant properties and burn rates; propellant density ρ_p was determined by using He-pycnometer

Prop. type	density ρ_p $[g/cm^3]$	a	n	Batch no.
HTPB1814	1.7747	2.196	0.399	G180242
HTPB0514	1.7223	2.473	0.420	G180243
HTPB0514	1.7163	2.504	0.415	G180245
HTPB0014Al2O3	1.7365	2.478	0.415	G180244

Table 4. Overview of the measurement techniques and targeted quantities. The quatities marked with an x can be determined; for the one in brackts (x), it is uncertain.

Method	Particle			Flow				
	Size	Temp.	Vel.	Temp.	Vel.	Press.	Spec.	other
FTIR		(x)		x			x	
UV-Vis		x					x	
AEM		x						
PIV			x					
HSS								x
DIPSD	(x)		(x)					
L2F			x					
APS	x							
RPC	x							
Press. trans.						x		
Gardon gauge								x
IR				x				(x)

in the frame of this project, AEM (*alumina emission measurement*) was adapted to the given requirements. The idea of AEM is to determine the phase state of the alumina particles inside the plume by using their thermal emission. These spectroscopic methods also provide information of the various species in the plume. For *particle image velocimetry* (PIV), a pulsed laser system illuminates the particles in the rocket exhaust plume. Cameras on either side perpendicular to the laser sheet capture the scattered light. The PIV camera targets as region of interest about one to two shock cells of the jet shock train. The camera for DIPSD (*direct imaging particle size determination*) is focused on a very small range (order of $4\,\mathrm{mm}$) of the exhaust plume. On the one hand, the intention of DIPSD is to directly gather data of the particle size by imaging glare points. On the other hand, it might also be used to deduce information about the velocity by cross-correlating particle images. The results of the velocimetry methods can then be cross-checked with highly accurate Laser-2-focus (L2F) measurements. High-speed schlieren (HSS) imaging concludes the list of measurement techniques for the exhaust plume. It is used to determine the density gradient field, and in particular, to visualize expansion and shock patterns in the flow field. The conditions of the rocket motor are monitored with two pressure sensors, and the ambient Mach number with a pitot-static/Prandtl tube. Note that all measurement equipment is put in boxes or wrapped to protect it from the corrosive exhaust plumes.

4. RESULTS AND DISCUSSION

In the next section, the experiences with the rocket motor are discussed. Then, in section 4.2, the measurement results are provided. These results are preliminary and not yet fully post-processed since, in the paper at hand, the focus lays on feasibility aspects. Further details will be presented in a follow-up publication.

4.1. Experiences regarding the Rocket Motor and the Protective Shield

This section discusses the experiences made with the current rocket motor such as with the glow plug, with the insulation, with the tungsten nozzle, and with the base plate.

Over the course of various measurement campaigns in VMK, the glow plug has replaced the pyrotechnic initiator as igniter for most test purposes at hand. During the setup procedure, the propellant is installed in such a way that it is pressed against the surface of the glow plug. The ignition is then triggered by supplying the glow plug with a sufficient amount of electrical energy. Ignition with the glow plug is safe, repeatable and reliable. It is safe since it evades the handling of sensitive pyrotechnic initiators. It is repeatable since the ignition takes place at about the same location. In other words, the ignition is not dependent on the location of the pyrotechnic initiator, which has usually been threaded from the top through nozzle into the combustion chamber. The glow plug is at a fixed location and, in contrast to the threaded pyrotechnic initiator, it cannot be moved due to aerodynamic forces imposed by the ambient wind tunnel flow. By using glow plugs, the number of misfires in the wind tunnel tests essentially dropped to zero.

As presented above, insulation was applied on the side and bottom wall of the propellant grain. An open question was whether the insulation withstands the heat load throughout tests. For that reason, the rocket motor was protected by an extra thermal protection layer consisting of a phenolic liner. Figure 5 shows both components after a representative test. It can be seen that both components barely suffer from the heat load and can be considered as intact. The carbon insulation rubber coat, which contained the propellant, is obviously deformed due to the heat, however it did not disintegrate. This is even more so for the phenolic liner, which even kept its characteristic original brownish color, meaning noteworthy pyrolysis of the material did not take place.

The behavior of the nozzle was the next open question in context of the behavior of rocket motor. In previous works, good experiences were gained with nozzles made of steel and a graphite nozzle inlet. However, since graphite is a brittle material, the surface of a graphite inlet suffers over time. To avoid that, it was decided to use tungsten as nozzle material for the tests at hand. Figure 6 shows one of the nozzles after some tests for which a dye penetrant dye inspection was carried out to find possible hairline fractures. As it can be seen by the pinkish color of the retraction dye, the tungsten nozzle actually features a hairline fracture upstream from the nozzle exit. It is assumed that the fractures are caused by thermal shocks. However, the fractures do not seem to penetrate the nozzle completely. During the tests, no leakage through the walls was observed neither in high-speed schlieren recordings nor in the particle image velocimetry recordings. Moreover, no residues of the plume were found on the nozzle after the tests. Despite these cracks, the tungsten nozzle itself appeared to be a good choice since the inner contour of the nozzle was maintained over all tests.

In the environment directly outside the combustion chamber is the base plate. The heat flux on the base plate is a quantity of interest for real flight configurations since, on the one hand, it prescribes the required insulation in the base region, and on the other hand, not much data is available for that. Thus, it was considered to measure the heat flux on a base plate made of PEEK by means of IR thermography. PEEK offers the advantage that the material properties (e.g. emissivity) are well-know and an adiabatic boundary condition can be assumed on the backside of the base plate due to the good insulating properties. However, as it can be seen in fig. 7, the PEEK material showed to be not suitable for that purpose. Due to the high heat loads it started to decompose. For the rest of the measurement campaign, black-colored alu-

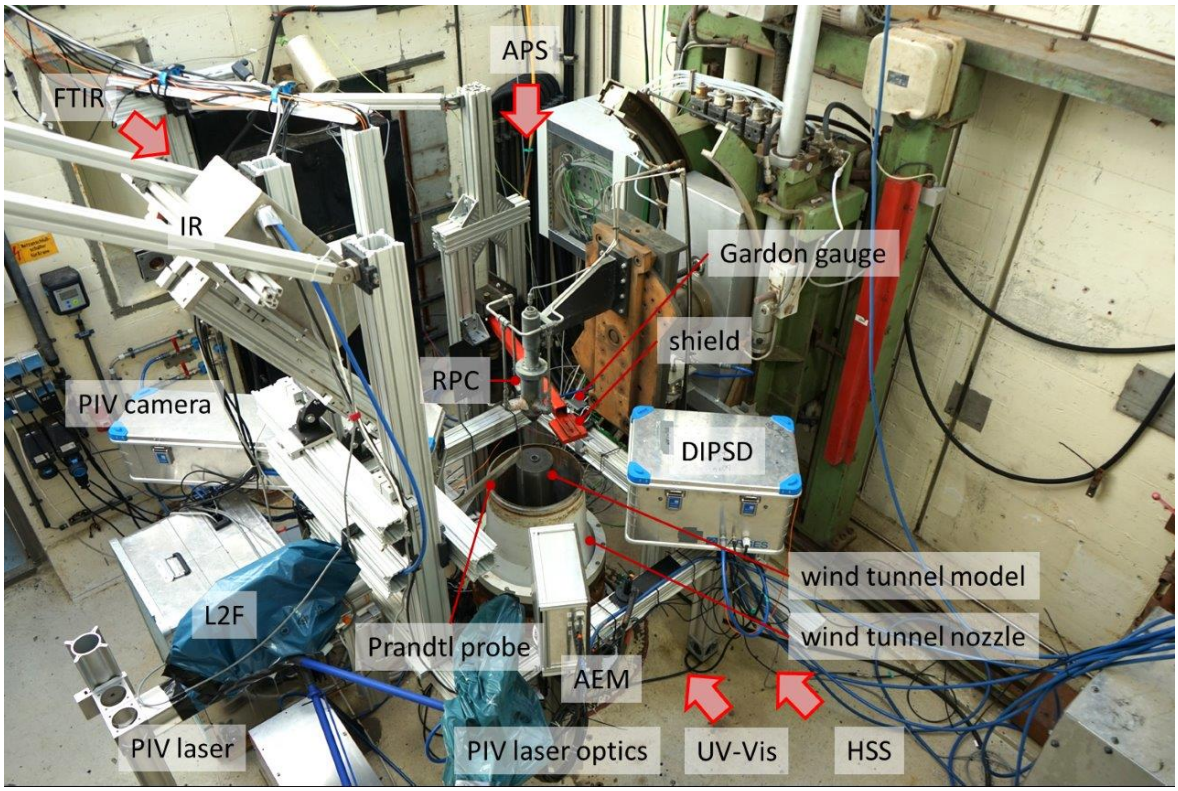

Fig. 3. Top view on the wind tunnel and measurement setup

minum was used.

In total, 26 successful hot firing tests were executed with the rocket motor. All of them used the same nozzle block of which one of the molybdenum parts failed during the 27th experiment. The corresponding part is marked as 5a in fig. 1, and fig. 8 shows an image of the damage after the last experiment.

In detail, this image depicts the top view into the rocket motor while it misses two parts of the nozzle block and the base plate (5b, 5c and 6 in fig. 1, respectively). Further, the damage is divided into two sections: section 1 relates to a cut out section and section 2 marks the remaining original section. The division into the two sections corresponds exactly to the form of the circlip (Seeger ring) used to hold the other two parts (5b and 5c) in place, meaning it actually appears as the circlip stamped out that part marked as section 1. Moreover, it is noteworthy that this part failed at chamber pressure of about $4.5\,\mathrm{MPa}$ after having withstood several times a pressure level in the range of about $10\,\mathrm{MPa}$. Thus, it seems very likely that the part failed due to thermal fatigue.

As a result, a threefold lesson should be kept in mind for the future: first, it is recommended to inspect the molybdenum parts exposed to thermal cycles with appropriate measures after a number predefined cycles, second, one might consider an improved thermal protection for that part, and third, one might consider the usage of a different material.

Apart from the rocket motor, open questions also concerned the protective shields before the execution of experiments. Four flat plates made of different materials were manufactured to protect the RPC most of the time from the hot exhaust plume. The different plates consisted of tungsten, molybdenum, graphite and aluminum oxide. However, only the tungsten plate was used since it proved to be suitable throughout all tests, and was correspondingly not exchanged. According to our visual inspections, the tungsten plate did not suffer from erosion, but exhibited a hairline crack by the end of the measurement campaign.

4.2. (Raw) Data of Measurements

In the following, a first glance is provided on the (raw) data of the various measurement methods for the purpose of showing the applicability.

4.2.1. Combustion Chamber Pressure

Before the tests, one of the questions concerned the behavior of the nozzle. Will the nozzle throat open up due to abrasion or due to high heat loads, will the nozzle throat remain constant or will some kind of deposition take place? This question is addressed in the following.

The pressure evolution for the HTPB0514 propellant

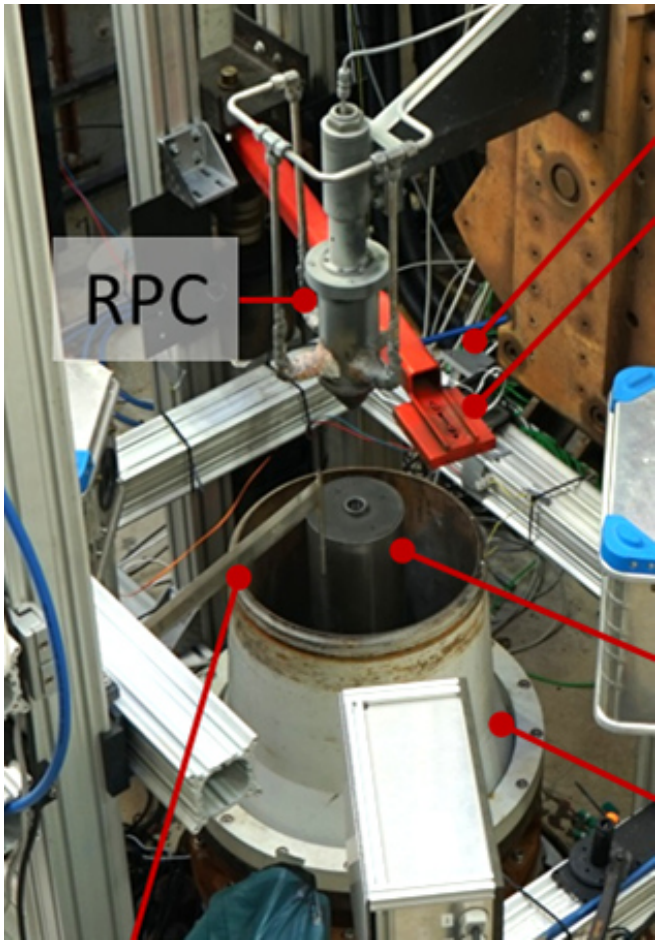

Fig. 4. Close-up of the wind tunnel model extracted from fig. 3

Fig. 6. Penetrant dye inspection of the tungsten nozzle

Fig. 5. Thermal insulation of the walls with carbon black insulation coat (left) and a phenolic liner (right) after usage

Fig. 7. (Burned) PEEK base plate after a hot firing test

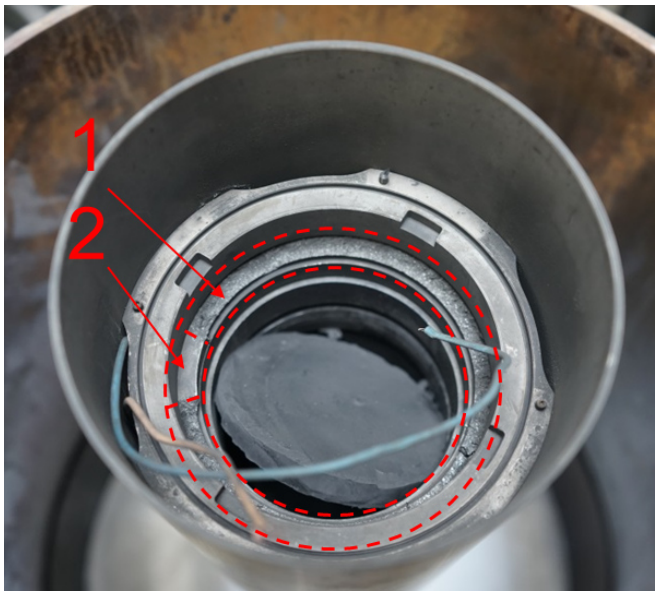

Fig. 8. Top view into the rocket motor after the nozzle block failure. Section 1 marks the stamped out section and section 2 marks the remaining original section.

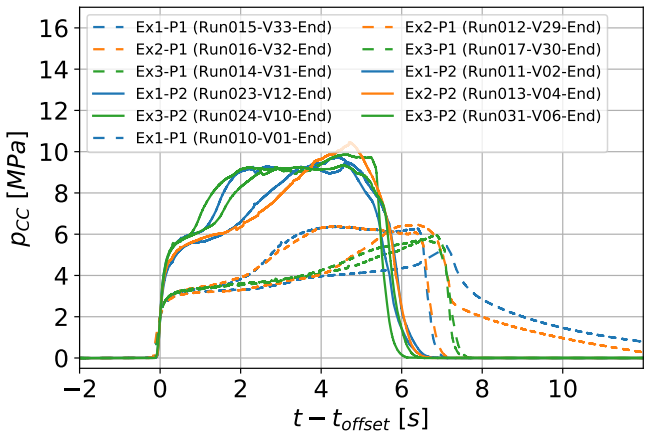

Fig. 9. Combustion chamber pressure evolution for the propellant with 5% aluminum (HTPB0514)

grain is provided in fig. 9. Initially, a constant pressure evolution was targeted, which was the reason for choosing an end-burner type grain. The constant pressure for that propellant grain was predicted to be at 2.9 MPa and 5.1 MPa. In fact, it can be seen that the pressure level directly after the ignition tends to converge to the predicted value. However, it can also be seen that with progressing time, the chamber pressure increases for all configurations. This is attributed to the deposition of alumina along the inner surface of the nozzle. Evidence for that is provided in fig. 10. The image shows a me that could be removed from the inside of the nozzle after the tests with HTPB0514. The outer contour of that deposition essentially corresponds to the inner contour of the truncated ideal contour (TIC) nozzle. Due to the predicted exhaust components and due to the whitish color, it appears safe to say that the deposition consists mainly of alumina. It seems like the deposition process is only repeatable within some limits, which explains the difference regarding the pressure evolution for the same configurations.

Further, the pressure evolution evidences that the deposition reaches an upper limit. After reaching that limit, part of the deposition might break of, which is indicated by small spikes notable over the course of the overall trend, e.g. for configuration Ex1-P2 or Ex3-P2. Note that the deposition's growth and break-up process at the nozzle exit was also notable in the high-speed schlieren, in the particle image velocimetry (fig. 13) and in the AEM (fig. 18) recordings. Last, the tail in the evolution of one of the two Ex2-P1- and Ex1-P1-cases shall be addressed. For that case, it is assumed that the burn surface is somewhat tilted, which could result in such a slowly decreasing pressure evolution since the burn surface would then advance in one of the bottom corners and provide less and less mass flux.

The pressure evolution of the HTPB0514Al_2O_3 with the innert alumina filler depicted in fig. 11 shows a behavior which is in contrast to the previous one. For that propellant type, a constant pressure level for the two smaller throat diameters of 3.0MPa and 5.3MPa was predicted, and as it can be seen, this is well matched. The finding regarding the rather constant pressure level is consistent with the overall observation after the experiments where no strong decomposition was found.

The pressure evolution of the remaining HPTB1814 grain is presented in fig. 12. The pressure evolution is in the order of the predicted range of 2.3 MPa, 4.0MPa, and 6.2 MPa, and in comparison to HTPB0514, rather constant. Deposition could be found after the tests, however to a lower degree again in comparison to HTPB0514. The occassional spikes in the pressure evolutions are attributed to the break-up of coated alumina chips during a run. Generally, the chamber pressure is at a lower level, which is easily explained by the lower burn rate (table 3) for that propellant, while using the same nozzle configurations for all propellants.

An impression regarding the thickness of the deposited material after the runs can be gained from table 5. It provides an averaged throat diameter before and after the run (*initial diam. vs. end diam.*) and the layer thickness after the run. However, please keep in mind that the values are difficult to take since the throat opening is not necessarily round, but rather fringy depending on the alumina decomposition process.

4.2.2. Particle Image Velocimetry (PIV)

A classical 2D-2C particle image velocimetry setup was applied for the purpose of determining the velocity distribution

Table 5. Throat diameter before and after a hot firing test

nozzle ID -	prop. ID -	part. -	initial diam. [mm]	end diam. [mm]	Δ diam. [mm]	run ID -
Ex1-P1	243	5% Al	7.75	6.50	~ 1.3	Run015-V33-End
Ex2-P1	243	5% Al	7.75	6.62	~ 1.1	Run016-V32-End
Ex3-P1	243	5% Al	7.75	6.15	~ 1.6	Run014-V31-End
Ex1-P2	243	5% Al	6.56	5.47	~ 1.1	Run023-V12-End
Ex3-P2	243	5% Al	6.56	5.60	~ 1.0	Run024-V10-End
Ex1-P1	245	5% Al	7.75	6.56	~ 1.2	Run010-V01-End
Ex2-P1	245	5% Al	7.75	6.16	~ 1.6	Run012-V29-End
Ex3-P1	245	5% Al	7.75	6.24	~ 1.5	Run017-V30-End
Ex1-P2	245	5% Al	6.56	5.60	~ 1.0	Run011-V02-End
Ex2-P2	245	5% Al	6.56	5.07	~ 1.5	Run013-V04-End
Ex3-P2	245	5% Al	6.56	5.40	~ 1.2	Run031-V06-End
Ex1-P1	244	5% Al_2O_3	7.75	7.62	~ 0.1	Run019-V35-End
Ex2-P1	244	5% Al_2O_3	7.75	7.50	~ 0.3	Run018-V34-End
Ex3-P1	244	5% Al_2O_3	7.75	7.51	~ 0.2	Run020-V36-End
Ex1-P2	244	5% Al_2O_3	6.56	6.47	~ 0.1	Run021-V19-End
Ex3-P2	244	5% Al_2O_3	6.56	6.48	~ 0.1	Run022-V17-End
Ex1-P1	242	18% Al	7.75	7.37	~ 0.4	Run025-V37-End
Ex2-P1	242	18% Al	7.75	7.34	~ 0.4	Run029-V39-End
Ex3-P1	242	18% Al	7.75	6.91	~ 0.8	Run026-V38-End
Ex1-P2	242	18% Al	6.56	6.43	~ 0.1	Run027-V26-End
Ex3-P2	242	18% Al	6.56	5.92	~ 0.6	Run028-V23-End
Ex3-P3	242	18% Al	5.74	5.20	~ 0.5	Run030-V25-End

Fig. 10. Deposition of alumina in the nozzle for the propellant 5% aluminum propellants HTPB0514 (after removal from the nozzle contour)

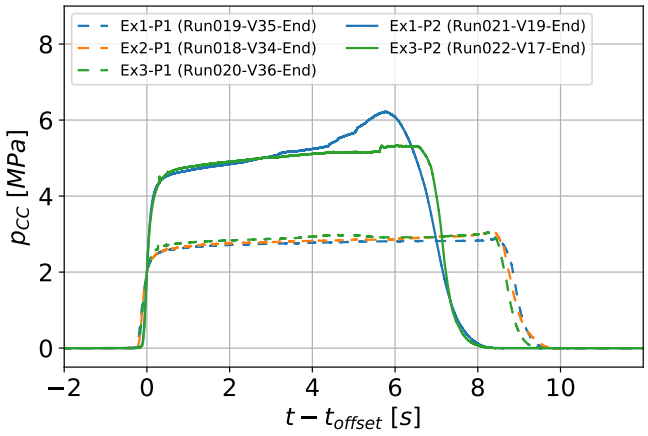

Fig. 11. Combustion chamber pressure evolution for the propellant with 5% alumina (HTPB0514Al2O3)

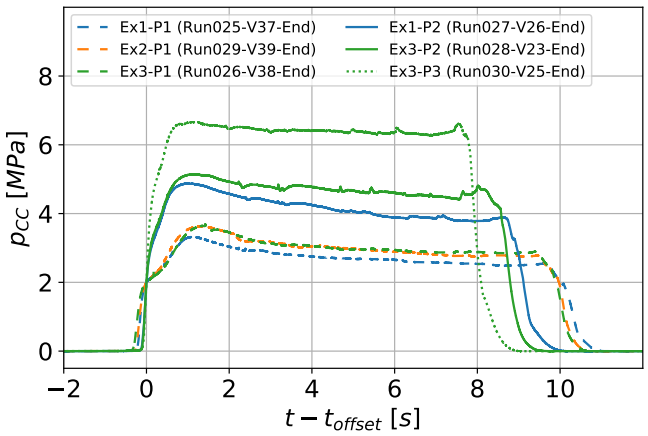

Fig. 12. Combustion chamber pressure evolution for the propellant with 18% aluminum (HTPB1814)

of the jet downstream from the nozzle exit. In more detail, the interconnecting equipment is based on a system by *LaVision* to which the main components, such as the *Ultra CFR Nd:YAG* laser by *Quantel/Big Sky Laser* and two *pco.edge 5.5* cameras by *PCO*, are connected.

Applying PIV measurements on a solid propellant exhaust jets is not a novelty (see [17]). However, it is quite unusual since it poses a very challenging environment due to the background irradiation due to the hot particles, the high velocities and the high temperature. Atypical is the usage of a bandwidth filter in the $532\,\mathrm{nm}$ range in front of the cameras to filter out the disturbing background irradiation.

Figure 13 shows raw, inverted intensity images as acquired during these measurements. The results all stem from the same nozzle configuration, which is Ex3-P2, while they differ with respect to the propellant type. The intention is to asses these images qualitatively with respect to their feasibility for PIV evaluation. Good PIV images show distinct particle images (here in black) and/or distinct patterns that can be cross-correlated with the second PIV image (which is not shown here).

It can be seen that the raw images for the tests with HTPB0514 and HTPB0014Al_2O_3 feature clear patterns in the shear layer, and distinct particle images can be detected in the core flow and distinct particles. Both, patterns and particles, can be used for cross-correlation evaluation. This is especially true for the case with HTPB0014Al_2O_3. Here, it appears as the (supposedly) inert particles are relatively large and remain the core flow, while finer particles can be accelerated laterally into the shear layer. For both configurations, a PIV evaluation is promising. This is not necessarily the case for the HTPB1814 for which the image appears to be relatively blurry without distinct particles. This can be explained, on the one hand, with the higher particle concentration, which is making the jet optically opaque, and on the other hand, with the stronger background irradiation of the particle. Thus, no velocity fields can be expected for the tests with HTPB1814.

4.2.3. Direct Image Particle Size Determination (DIPSD)

The setup used for DIPSD relies on the same laser and interconnecting equipment as for the PIV setup. However, to provide a better spatial resolution the *PCO1600* camera by *PCO* was equipped with the *Model K2 DistaMax* lens system by *Infinity Photo-Optical*. As a result, the field of view for this setup was $3.4\,\mathrm{mm} \times 4.0\,\mathrm{mm}$.

An exemplary image is provided in fig. 14. The original idea was to capture glare points for the particle size determination. However, this exemplary image does not exhibit glare points, thus further investigations must show if this is actually possible with this setup. Nevertheless, it might also be used to gain spatially highly resolved velocimetry data just by applying a standard PIV evaluation on the raw data set. Apart from PIV and L2F, this would be the third measurement technique providing insights into the velocity distribution of the rocket exhaust plume, and as such, also useful for cross-checks.

4.2.4. Laser-2-Focus (L2F)

In short, the laser-2-focus measurement method is based on a time-of-flight measurement of a particle captured between the foci of two laser beams [18, 19, 20, 21, 22, 23, 24]. The velocity is determined by means of the distance between the two foci and the corresponding time-of-flight. Exemplary results of which for a location downstream of the hot exhaust jet for the three propellant types are given in fig. 15. The graph shows the velocity of the particles as function of the corresponding counts. In total, 2000 (randomly selected) samples are evaluated here. The velocity itself must still be assessed in context with the flow topology. Of interest now is only the feasibility of the measurements, and it can be seen that data can be extracted from tests with all three propellant types. Taking into account that no PIV evaluation appears to be possible for the HTPB1814 propellant, this finding is unexpected. The L2F measurement, in that case, still captures a significant amount of events, ergo valid data, for this optically rather dense flow, and thus unexpectedly provides additional information of the jet.

4.2.5. Spectroscopic Measurements: FTIR, UV-Vis and AEM

UV-Vis emission spectroscopy was performed using an *OceanOptics USB2000* spectrometer covering a spectral range from 200 to $850\,\mathrm{nm}$ (relative intensity calibration valid from $500\,\mathrm{nm}$ upwards) in a cylindrical volume $30\,\mathrm{mm}$ above the nozzle exit and of about $7\,\mathrm{mm}$ diameter. Figure 16 depicts a typical UV-Vis emission spectrum, showing the plume emission of Run012-V29-End at $1.95\,\mathrm{s}$. The particle phase grey body radiation as well as the atomic emission lines of Na and K is visible. Also the inferring emission lines of

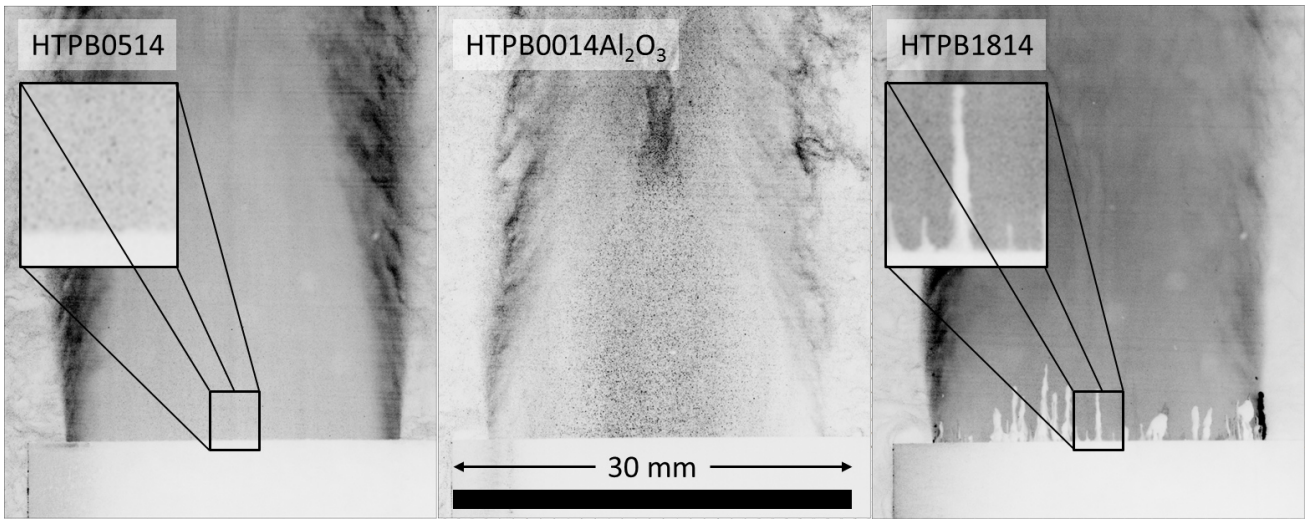

Fig. 13. Randomly selected (inverted) raw intensity images of the PIV measurements for tests with the Ex3-P2 nozzle and with the HTPB0514 (left, Run031-V06-End), $\mathrm{HTPB0014Al_2O_3}$ (mid, Run022-V17-End), and HTPB1814 (right, Run028-V23-End) propellant grain. Note that the streaks visible for the HTPB1814-case are the result of externally growing alumina depositions along the boundary of the jet.

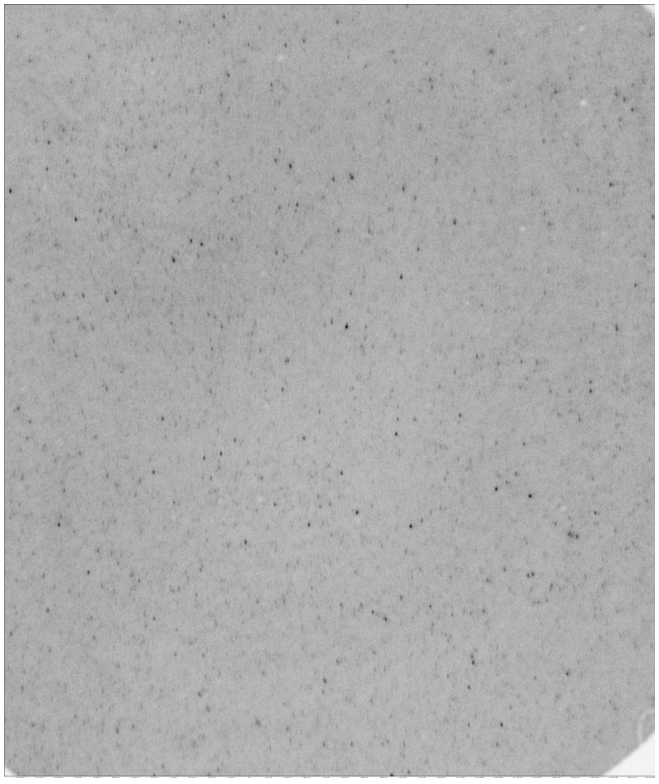

Fig. 14. Randomly selected (inverted) raw intensity images of the DIPSD measurements with the Ex3-P2 nozzle and with the HTPB0514 propellant grain (Run031-V06-End). The image/field of view corresponds to $3.4\,\mathrm{mm} \times 4.0\,\mathrm{mm}$.

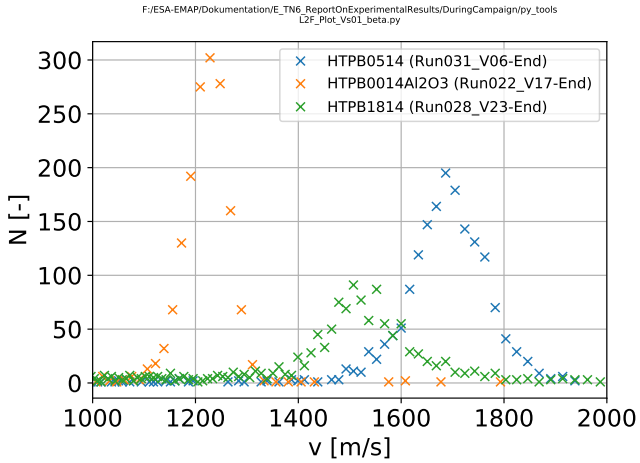

Fig. 15. L2F velocity measurement of the particles in the supersonic exhaust jet

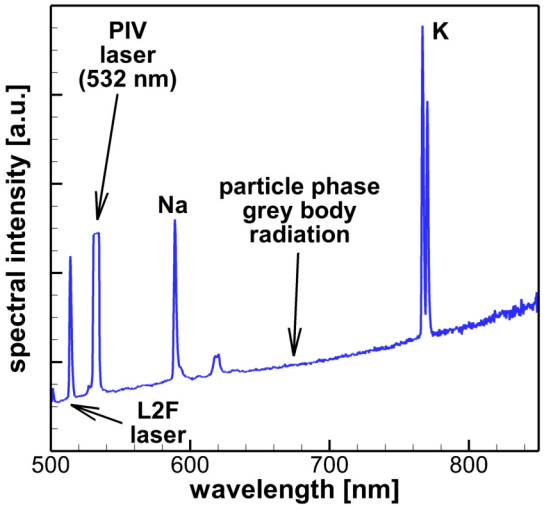

Fig. 16. UV-Vis emission spectrum of the rocket exhaust plume (5% aluminum, Run012-V29-End)

both L2F and the PIV laser system can be seen. The particle phase emission will be evaluated to get the history of particle emission intensity and of particle grey body temperature.

Fourier transform IR (FTIR) emission spectroscopy was performed using an *ABB MR 304* covering a spectral range from 1 to 8 μm in a cylindrical volume 30 mm above the nozzle exit and of about 25 mm diameter. Figure 17 depicts a typical IR emission spectrum, showing the molecular emission lines of CO2, CO, H2O and HCl during Run031-V06-End. The emission lines of HCl will be used to determine the gas temperature.

Alumina emission measurement (AEM) is effectively a position resolving two-color pyrometer. It is an in house development, build from two cameras taking pictures at 630 nm and 700 nm, respectively. A dichroic mirror at 650 nm splits the image into two separate paths, which then are filtered by bandpass filters of 10 nm FWHM. A detailed publication will follow. From the intensity ratio of two synchronized images particle (fig. 18) the temperature and particle density distribution of the plume will be derived. In fig. 18 at the top, the protective shield for the RPC is visible. At the nozzle exit the externally growing alumina depositions along the boundary of the jet can be observed, which were also observed in the PIV imaging (fig. 13)

4.2.6. *High-Speed Schlieren (HSS)*

Figure 19 and fig. 20 show an instantaneous and an averaged high-speeds schlieren image, respectively. For the acquisition, a Z-type schlieren setup readily installed in VMK was used and the images were recorded with a *Photron Fastcam*

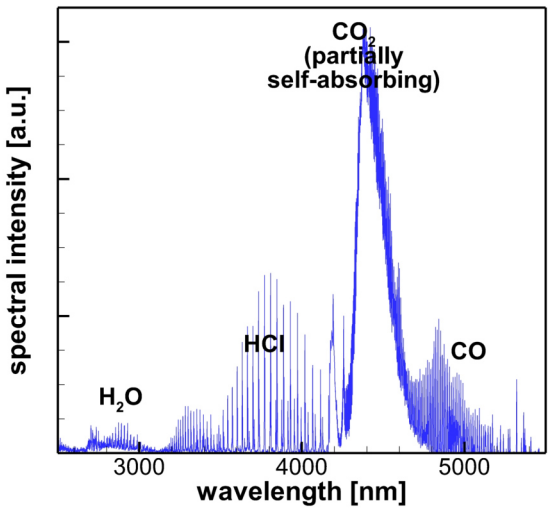

Fig. 17. Fourier transform IR (FTIR) emission spectroscopy of the rocket exhaust plume (Run031-V06-End)

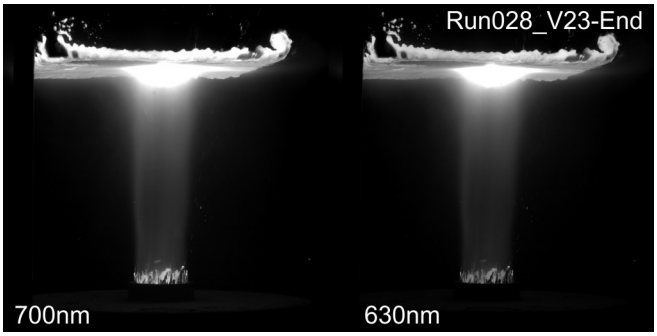

Fig. 18. Raw images at 630 nm and 700 nm taken by the AEM for a test with 18% aluminum (Run028-23-End)

SA-X2 type 1080K-M4. The main focus of the HSS recordings regards the monitoring of the experiments, on the one hand, and on the other hand, the extraction of the flow topology of the plume. In fact, features of the flow topology can be observed in fig. 20.

The image features a shock evolving from the right side of the nozzle which is then reflected at the shear layer. This feature is more distinct on the left side which is attributed to the orientation of the knife edge. The vertically aligned knife edge introduced a gradient in the lateral direction. On top of that, the highly turbulent wake flow notable in fig. 19 has an impact on the signal-to-noise ratio of the mean flow features, which also impede the isolation of mean flow features. Next, the propellant used for this test contains 5% aluminum. This additionally decreases the transmissivity inside the plume. Nevertheless, the presence of such a shock system is notable.

Further, the highly turbulent flow of various scales indicate a strong heating of the fluid of the base region. This is in contrast to tests with a cold exhaust jet (not shown here) where the flow in the base region is typically less turbulent. In other words, in comparison to cold jet tests, different conditions are imposed in the base region due to the presence of a hot jet.

4.2.7. Aerodynamic Particle Sizer (APS)

Apart from the RPC, a second system has been integrated in the wind tunnel to capture the particle size distribution. Namely, it is the *Aerodynamic Particle Sizer APS 3321* by *TSI* in combination with the diluter *3302A*. The particles are extracted from the nozzle exhaust plume far downstream (about $4\,\mathrm{m}$) from the jet.

The APS is equipped with two methods to assess the particle size. One method is based on the aerodynamic acceleration through a nozzle, and a second method, which is based on the scattering of laser light. In combination, the results can be correlated and invalid particle clusters can be removed. Invalid particle or particle clusters would appear as outliers when the scattering intensity is related to the particle size. As fig. 21 shows, this is not the case for the current measurements captured with the APS. The graph depicts the Stokes corrected aerodynamic particle size distribution for alumina ($\rho_{Al_2O_3} = 3.95\,\mathrm{g/cm^3}$). At that instant in time, it appears as most of the particles can be found in the sub-micrometer range at about $0.7\,\mu\mathrm{m}$

4.2.8. Gardon Gauge

The radiative heat flux from the exhaust plume to its surrounding components is of special interest especially for the base region. For one of the rare experiments without protective shield, fig. 22 provides that quantity (low-pass filtered) in context of combustion chamber pressure for an experiment with 5% aluminum. The strong correlation to the start-up of the motor, indicated by the pressure increase, provides a strong foundation for the validity of the radiative heat flux data. After about $\Delta t = 5\,\mathrm{s}$, a strong increase can be found, which is believed to correlate with the radiative flashes noted in the high-speed schlieren measurements towards the end of the experiments. It might be the result of chipped alumina depositions or of additional components being released and burned in the combustion chamber towards the end of a run. Further open questions such as the offset after the motor's shut-down run will be assessed in future analysis. For now, the approach has shown that measurements can be taken in such a manner.

4.2.9. IR-thermography (IR)

The IR recording in fig. 23 shows why the PEEK plate (fig. 7) did not withstand the heat flux in the base region. For orientation, only a section of the base plate is shown and the edge of the main cylinder (edge partially visible) is on the left side while the nozzle is on right side. The dots on the base plate represent markers which will be used later for scaling and image distortion. Further, the images were recorded with the *ImageIR 8300* camera by *InfratTec*.

It can be seen that the black-colored aluminum plate reaches an average temperature above $400\,\mathrm{K}$ for this instant in time while the hotter spots can obviously be found at the section surrounding the nozzle. Keep in mind that transient flow conditions, like start-up or shut-down, might impose even higher heat loads since the hot gases coming from the nozzle are then more prone to be sucked into the recirculation region.

4.2.10. Rocket Plume Collector (RPC)

The *rocket plume collector* has been developed in the frame of ESA-EMAP project and it is depicted in fig. 4. In short, particles are sampled through an opening at the tip of the RPC, which are then internally slowed down and quenched with a quenching liquid. Its objective is to deduce the particle size in a post-processing step. The first preliminary results can be accessed in ref. [25]. Further insights to the working mechanism and details to operational range can be extracted from ref. [26, 27, 28, 29, 30].

5. LESSONS LEARNED

Lessons learned regarding the rocket motor:

- The glow plug as ignition device worked reliably.
- Carbon black has proven be a suitable thermal insulator.
- Phenolic liners have already been used as thermal insulator in the past and will be used for comparable applications in the future again.

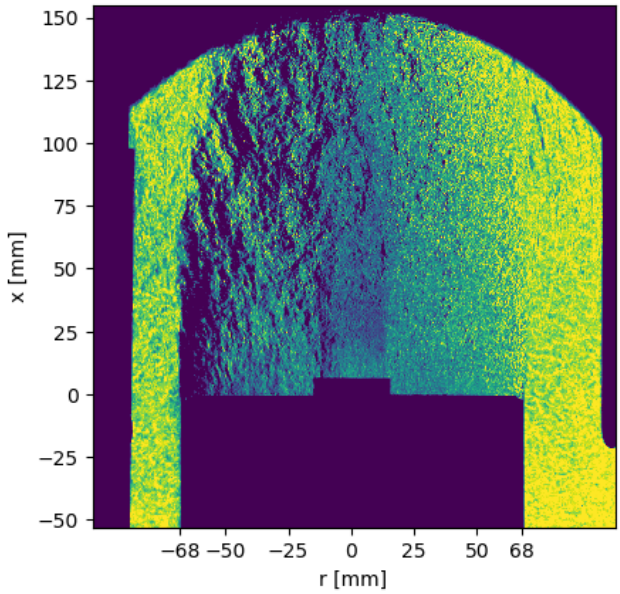

Fig. 19. False color representation of an instantaneous high-speed schlieren image for a test with 5% aluminum (Run031-V06-End)

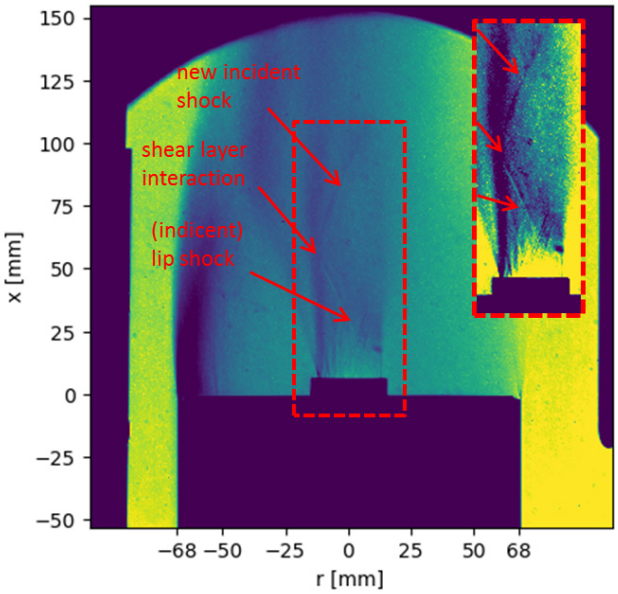

Fig. 20. False color representation of an averaged high-speed schlieren image for a test with 5% aluminum (Run031-V06-End)

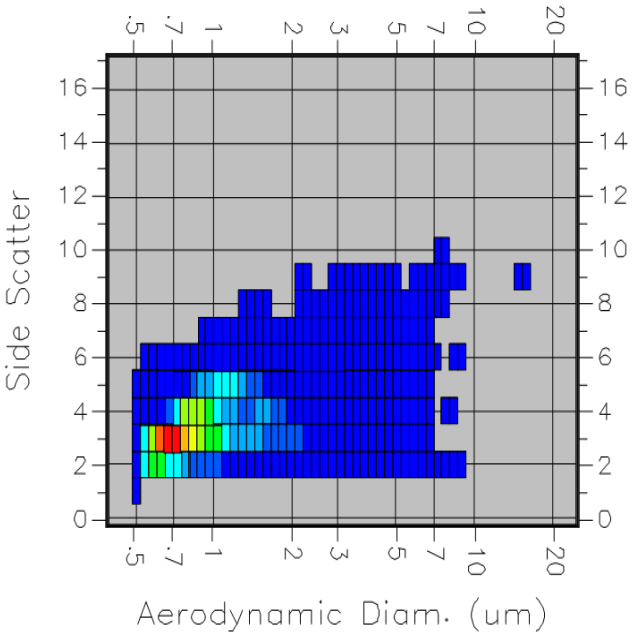

Fig. 21. Correlation plot between aerodynamic particle size and laser light scattering measured with the APS at a randomly picked point in time for a test with 5% aluminum (Run031-V06-End)

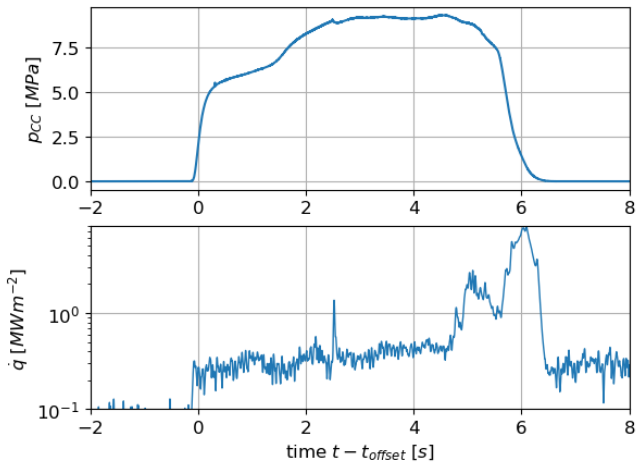

Fig. 22. Combustion chamber pressure in comparison with the (low-pass filtered) radiative heat flux from the exhaust plume of a 5% aluminum-content propellant measured by a Gardon gauge (Run031-V06-End)

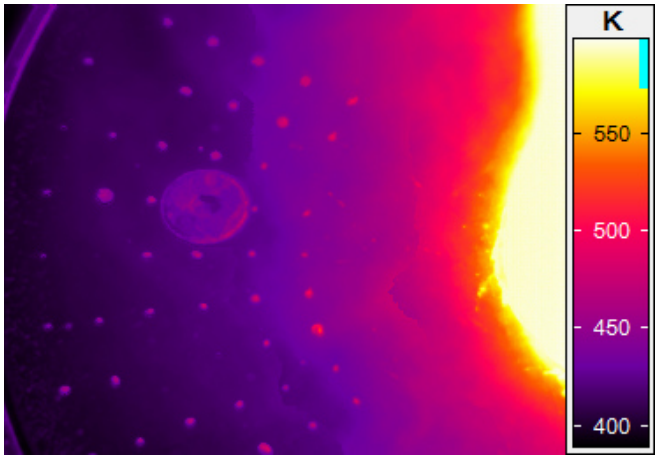

Fig. 23. IR recording of the base plate for a test with 5% aluminum (Run031-V06-End) at a randomly picked point in time

- A different approach must be followed for the failed molybdenum part. The options are as following: (1) Acquiring a better understanding of the material characteristics to cyclical heat and pressure loads, (2) implement regular, non-destructive metallurgic inspections, (3) integrate a thermal protection system at that section, and/or (4) reconsider the material choice.

- Tungsten might have to be reconsidered as material for the nozzles since microcracks were detected already after a single run. Nevertheless, the corresponding nozzles have shown to withstand several further tests with no signs of leakage and without any constraints. However, it is difficult to justify such an outcome as baseline for future tests.

- When using propellants with 5% aluminum, the nozzle throat diameter decreases over one run due to clogging causing a corresponding increase of the chamber pressure.

- The protective shield made of tungsten was able to withstand the heat and pressure loads for more than 20 runs.

Lessons learned regarding the applied measurement techniques:

- Velocimetry measurements methods such as PIV, L2F and the off-use DIPSD appear to be suitable to derive velocity data in a solid exhaust plume. For an optically relatively dense plume (18% aluminum content), only L2F managed to capture valid data.

- Spectroscopic measurement methods reliably provided intensities as function of the wavelength. These results are promising to derive the temperature distribution of gas and particles.

- Well-established measurement methods such as HSS, IR and pressure measurements have fulfilled their expectations. Thus, data regarding flow topology, the temperature of the base plate, and the chamber pressure evolution is accessible.

- The Gardon gauge acquired data attributable to the radiative heat flux of the plume.

- Particles were successfully extracted from the hot exhaust plume by means RPC probe [25].

- Further downstream from the nozzle exhaust, the APS reliably gathered data, which can be used for cross-checks with the RPC.

6. CONCLUSIONS AND OUTLOOK

The current study presents the activities in the frame of ESA-EMAP for the characterization of a rocket exhaust plume. In the frame of this report, aspects to the functionality of rocket motor itself and the applicability of the various measurement techniques were discussed. Despite the fact that some components, such as the molybdenum nozzle block, require improvements the rocket motor has proven its overall functionality. Further, on a first glance, the measurement results are very promising. Thus, as next steps, the individual measurements will be analyzed in depth and in context with each other to extract more details regarding the particles in a rocket exhaust plume.

Acknowledgments

Financial support has been provided by the European Space Agency (ESA) in the framework of the project *Experimental Modelling of Alumina Particulate in Solid Boosters (ESA-EMAP)*. Further, thanks a lot to the colleagues and the staff for their support!

7. REFERENCES

[1] O. Schmid, J.M. Reeves, J.C. Wilson, C. Wiedinmyer, C.A. Brock, D.W. Toohey, L.M. Avallone, A.M. Gates, and M.N. Ross, "Size-resolved particle emission indices in the stratospheric plume of an Athena II rocket," *Journal of Geophysical Research: Atmospheres*, vol. 108, no. D8, 2003.

[2] C.H. Jackman, D.B. Considine, and E.L. Fleming, "In situ measurement of the aerosol size distribution in stratospheric solid rocket motor exhaust plumes," *Geophysical Research Letters*, vol. 25, pp. 907–910, 1998.

[3] Martin N Ross, Philip D Whitefield, Donald E Hagen, and Alfred R Hopkins, "In situ measurement of the aerosol size distribution in stratospheric solid rocket motor exhaust plumes," *Geophysical Research Letters*, vol. 26, no. 7, pp. 819–822, 1999.

[4] F.S. Simmons, *Rocket Exhaust Plume Phenomenology*, Aerospace Press El Segundo, CA, 2000.

[5] B.H. Goethert, "Base Heating Problems of Missiles and Space Vehicles," *ARS Paper*, pp. 1666–61, 1961.

[6] K. Kinefuchi, K. Okita, I. Funaki, and T. Abe, "Prediction of In-Flight Radio Frequency Attenuation by a Rocket Plume by Applying CFD/FDTD Coupling," *49th AIAA/ASME/SAE/ASEE Joint Propulsion Conference, July 14 - 17, 2013, San Jose, CA, AIAA 2013-3790*, 2013.

[7] K. Triesch and E.-O. Krohn, *Die Vertikale Meßstrecke der DFVLR in Köln-Porz (Stand 1986), DFVLR-Mitt. 86-22*, Wissenschaftliches Berichtswesen der DFVLR, ISSN 0176-7739, Postfach 906058, 5000 Köln 90, 1986.

[8] Aerospace Center German DLR, "Vertical Test Section Cologne (VMK), Supersonic and Hypersonic Technology Department," 2019.

[9] Dominik Saile, Daniel Kirchheck, Ali Gülhan, and Daniel Banuti, "Design of a Hot Plume Interaction Facility at DLR Cologne," in *Proceedings of the 8th European Symposium on Aerothermodynamics for Space Vehicles*, 2015.

[10] John David Anderson, *Modern compressible flow: with historical perspective*, vol. 12, McGraw-Hill New York, 1990.

[11] A. Ponomarenko, "RPA-Tool for Rocket Propulsion Analysis," in *Space Propulsion Conference*, 2014.

[12] Dominik Saile, Viktor Kühl, and Ali Gülhan, "On the subsonic near-wake of a space launcher configuration without jet," *Experiments in Fluids*, vol. 60, no. 4, pp. 50, Mar 2019.

[13] Dominik Saile, Viktor Kühl, and Ali Gülhan, "On the Subsonic Near-Wake of a Space Launcher Configuration with Jet," *Experiments in Fluids*, accepted 2019.

[14] Dominik Saile, Viktor Kühl, and Ali Gülhan, "On Subsonic Near-Wake Flows of Various Base Geometries," in *13th International Symposium on Particle Image Velocimetry (ISPIV 2019), July 22.-24., 2019*, 2019.

[15] Dominik Saile, *Experimental Analysis on Near-Wake Flows of Space Transportation Systems*, Ph.D. thesis, submitted in February, 2019 at the Rheinisch-Westfälische Technische Hochschule Aachen, 2019.

[16] Daniel Kirchheck, Dominik Saile, and Ali Gülhan, "Spectral Analysis of Rocket Wake Flow-Jet Interaction by Means of High-speed Schlieren Imaging," in *8th European Conference for Aeronautics and Space Sciences (EUCASS)*, 1–4 July, Madrid, Spain, 2019.

[17] B. J. Balakumar and R. J. Adrian, "Particle-image velocimetry measurement in the exhaust of a solid rocket motor," *Experiments in Fluids*, vol. 36, no. 1, pp. 166–175, Jan 2004.

[18] R. Schodl, "Laser-two-focus velocimetry, in: Advanced instrumentation for aero engine components," in *AGARD-CP-399, paper 7, Philadelphia*, 1986.

[19] R Schodl and W Förster, "A multi colour fiber optic laser two focus velocimeter for 3-dimensional flow analysis," in *24th Joint Propulsion Conference*, 1988, p. 3034.

[20] R. Schodl, W. Förster, and M. Beversdorff, *Neue Entwicklungen beim L2F-Verfahren. Berichte aus der Lasermeßtechnik "Lasermethoden in der Strömungsmeßtechnik"*, A. Leder (Hrsg.), Verlag Shaker, 1995.

[21] W Forster, "Laser-2-focus data analysis using a nonlinear regression model," in *ICIASF'95 Record. International Congress on Instrumentation in Aerospace Simulation Facilities*. IEEE, 1995, pp. 22–1.

[22] S Ardey, L Fottner, M Beversdorff, and H Weyer, "Laser-2-focus measurements on a turbine cascade with leading edge film cooling," in *AGARD conference proceedings*. AGARD, 1998, pp. 12–1.

[23] M Beversdorff, L Matziol, and C Blaha, "Application of 3d-laser two focus velocimetry in turbomachine investigations," in *AGARD conference proceedings*. AGARD, 1998, pp. 13–1.

[24] W Förster, G Karpinsky, H Krain, I Röhle, and R Schodl, "3-component doppler laser-two-focus velocimetry applied to a transonic centrifugal compressor," in *Laser Techniques for Fluid Mechanics*, pp. 55–74. Springer, 2002.

[25] Filippo Maggi, Stefania Carlotti, Galfetti, Dominik Saile, Ali Gülhan, Mattias Liljedahl, Tobias Langener, and Jeroen van den Eynde, "Determining the particles size in solid rocket motor plume," in *International Conference on Flight vehicles, Aerothermodynamics and Re-entry Missions and Engineering (FAR)*, 2019.

[26] Stefania Carlotti, Filippo Maggi, Alessandro Ferreri, Luciano Galfetti, Riccardo Bisin, Dominik Saile, Ali Gülhan, Christopher Groll, and Tobias Langener, "Development of an intrusive technique for particles collection in rockets plume," *Acta Astronautica*, vol. 158, pp. 361 – 374, 2019.

[27] Stefania Carlotti, Filippo Maggi, Stefano Dossi, Riccardo Bisin, Luciano Galfetti, Dominik Saile, Ali Gülhan, Christopher Groll, and Tobias Langener, *Overview of a Supersonic Probe for Solid Propellant Rocket CCP Collection*.

[28] Filippo Maggi, Riccardo Bisin, Alessandro Ferreri, Stefania Carlotti, Luciano Galfetti, Christopher Groll, Tobias Langener, et al., "Development of a probe for particle collection in high-temperature, supersonic flow: Application of quasi-1d engineering model and 2d axisymmetric cfd," in *7th European Conference for Aeronautics and Space Sciences*, 2017, pp. 3–7.

[29] Stefania Carlotti, Alessandro Ferreri, Riccardo Bisin, Filippo Maggi, Luciano Galfetti, Dominik Saile, Ali Gülhan, and Tobias Langener, "Development of a probe for particle collection in high-temperature, supersonic flow: Conceptual and detailed design," in *7th European Conference for Aerospace Sciences*, 2017.

[30] Filippo Maggi, Stefania Carlotti, Galfetti, Dominik Saile, Ali Gülhan, Mattias Liljedahl, Jeroen van den Eynde, and Tobias Langener, "Particle size in srm plume: Assessment of collection method," in *8th European Conference for Aeronautics and Aerospace Sciences (EUCASS)*, 2019.